Photoionization of Nitrile-substituted Naphthalene and Benzene: Cation Spectroscopy, Photostability, and Implications for Photoelectric Gas Heating

Madhusree Roy Chowdhury, Gustavo A. Garcia, Helgi R. Hrodmarsson, Jean-Christophe Loison, Laurent Nahon

The Astrophysical Journal, 963:29 (12pp), 2024 March 1 https://doi.org/10.3847/1538-4357/ad16d9

Photoionization of Nitrile-substituted Naphthalene and Benzene: Cation Spectroscopy, Photostability, and Implications for Photoelectric Gas Heating

Madhusree Roy Chowdhury[1], Gustavo A. Garcia[1], Helgi R. Hrodmarsson[2], Jean-Christophe Loison[3], and Laurent Nahon[1]
[1] Synchrotron SOLEIL, L'Orme des Merisiers, Départementale 128, Saint Aubin F-91190, France; madhusree.roy-chowdhury@synchrotron-soleil.fr
[2] Univ Paris Est Creteil and Université Paris Cité, CNRS, LISA UMR 7583, 94010 Créteil, France
[3] Université Bordeaux, CNRS, Bordeaux INP, ISM, UMR 5255, Talence F-33400, France
Received 2023 October 17; revised 2023 December 12; accepted 2023 December 17; published 2024 February 26

Abstract

We investigate the vacuum ultraviolet (VUV) photodynamics of gas phase 1- and 2-cyanonaphthalene and cyanobenzene, recently detected in the Taurus molecular cloud, by combining synchrotron radiation and a double imaging electron/ion coincidence setup. The high-resolution threshold photoelectron spectra (TPES) of all three molecules are obtained experimentally from which the adiabatic ionization energies are reported with very high accuracy, particularly for 2-cyanonaphthalene, for which no data exist at this level of precision. Theoretical calculations are performed to compare with the TPES for the ground electronic state of the cations. Furthermore, the different features observed in the extended TPES have been assigned to the different molecular orbitals with the help of the outer valence Green's function calculations. The present experiments also shed light on the kinetic energy distribution of the photoelectrons as a function of the incident photon energy, to describe their contribution to the photoelectric heating effect in the interstellar medium. In this context, we show how kinetic energy distributions can be obtained from our data for any given photon energy, such as the omnipresent Lyα line, or any given interstellar radiation field (ISRF). In addition, from the total ion yields, we estimate the photorates for a few ISRFs. Finally, we discuss the photodissociation of the two cyanonaphthalenes, quoting the activation energies of the dissociation channels with the help of Rice–Ramsperger–Kassel–Marcus modeling. It is observed that CN substitution does not cause any appreciable change to the VUV dissociative photoionization relaxation channel.

Unified Astronomy Thesaurus concepts: Interstellar medium (847); Photoionization (2060); Photoelectron spectroscopy (2097)

1. Introduction

Polycyclic aromatic hydrocarbons (PAHs) have been accepted for decades to be one of the key species in the interstellar medium (ISM), acting as reservoirs of carbon and being the most abundant organic molecules in space (Leger & Puget 1984; Allamandola et al. 1985; Tielens 2008). Interstellar PAHs can contain up to about 20% of the cosmic carbon budget and play a significant role in the temperature, energy, and ionization balance of the ISM (Verstraete 2011). The mid-infrared emission spectra seen from different Galactic sources like planetary nebulae (Ohsawa et al. 2012; Cox et al. 2015; Boersma et al. 2018), diffuse and dense clouds (Joblin et al. 1992; Wakelam & Herbst 2008), photodissociation regions (Rapacioli et al. 2005; Montillaud et al. 2013; Croiset et al. 2016), H II regions (Stock & Peeters 2017; Topchieva et al. 2018), reflection nebulae (Sellgren et al. 2007; Boersma et al. 2016; Knight et al. 2021), protoplanetary disks (Maaskant et al. 2014; Zhang et al. 2017; Taha et al. 2018), and extragalactic sources like starburst galaxies (Brandl et al. 2006; Canelo et al. 2018), H II regions in the Magellanic Clouds (Li & Draine 2002; Oey et al. 2017), submillimeter galaxies (Menéndez-Delmestre et al. 2009), and Seyfert galaxies (García-Bernete et al. 2022), bearing features in the 3–20 μm spectral range, have been attributed to PAH molecules. In the low-density part of the ISM, PAHs are continuously exposed to vacuum ultraviolet (VUV) radiation emitted by hot stars. A photoexcited PAH molecule can relax via different channels like photoionization, photodissociation, or radiative processes. Aromatic infrared emission bands (AIBs) are the result of radiative cooling where the PAHs absorb VUV photons and relax by IR emission. It is postulated that large PAHs with 50 or more carbon atoms are the main carriers of AIBs (Tielens 2011). These molecules also have absorption bands in the visible and UV region, and their cationic forms are favorable candidates for diffuse interstellar bands (Steglich et al. 2011). In the case of smaller PAHs, ionization and fragmentation are the leading relaxation pathways (Leach 1986; Jochims et al. 1994). In photodissociation regions (PDRs), depending on the radiation field intensity, PAHs (especially large ones) are expected to be not only singly but also doubly ionized (Bakes et al. 2001).

Although PAHs are key species in the ISM, contributing enormously to the photophysics and the photochemistry of the ISM, individual molecular identification in the astrophysical environment is challenging due to their, at best, weak dipole moments. Substituted PAHs with polar groups such as CN are therefore more amenable for detection and, recently, McGuire and co-workers have detected the two isomers of cyano-naphthalene $C_{10}H_7CN$ (CNN; see Figure 1) in the cold Taurus molecular cloud (TMC-1) using a radio telescope (McGuire et al. 2021), the first ever definitive identification of a PAH molecule. In 2018, the same team detected cyanobenzene in TMC-1 (McGuire et al. 2018). Detection of another PAH, the indene (Burkhardt et al. 2021a; Cernicharo et al. 2021) and

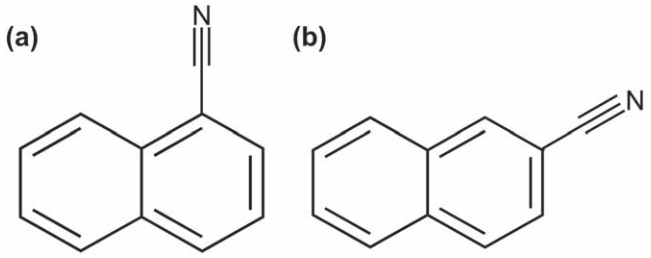

Figure 1. Molecular structure of cyanonaphthalene (a) 1-CNN and (b) 2-CNN.

cyano-indene (Sita et al. 2022) in the same molecular cloud, provided information on the relative abundances of pure and substituted PAHs, with a ratio of pure to cyano-indene of 40 and chemical models predicting a ratio of 20 for $C_{10}H_8/C_{10}H_7CN$ (Sita et al. 2022). Since cyanides are known to be present abundantly in various interstellar environments (Bottinelli et al. 2004; Belloche et al. 2014), their detection confirms the large abundance of PAHs in interstellar environments. Cyano-substituted PAHs can be formed by a barrierless reaction between the PAH and the CN radical, as has already been investigated for cyanobenzene (Lee et al. 2019). In addition to TMC-1, benzonitrile has also been detected in four other prestellar sources (Burkhardt et al. 2021b). From these observations, it may be inferred that TMC-1 is a rich inventory of PAH molecules and that exploiting the cyanide trump card yields information on the presence of pure PAH in interstellar environments. Apart from TMC-1, very recently Agúndez et al. (2023) have reported the presence of PAHs in other cold clouds, which have an abundance of carbon chains. Although the far-UV photons do not penetrate deep inside the dark molecular clouds, and thus the molecules residing in these regions are well shielded, the ones near the cloud edges and in other PDR regions are exposed to a harsh VUV radiation field. However, the PAHs inside the clouds are exposed to a weak, but nonzero, VUV radiation field generated by the Lyman and Werner bands of hydrogen which is continually excited by energetic cosmic rays penetrating the dark clouds (Prasad & Tarafdar 1983). The cosmic rays ionize H_2 molecules, generating a cascade of re-scattered electrons that further participate in producing excited H atoms that radiatively decay (Cravens & Dalgarno 1978). The cosmic rays continuously replenish the cloud with reactive radicals and ions, playing a significant role in driving the chemistry inside the dark clouds (Dalgarno 2006).

It is therefore important for modeling the abundance of cyano-PAHs and, by proxy, PAHs, to perform laboratory measurements on their VUV photochemistry, including ionization energies and cation dissociation thresholds. Different studies exist on cyanonaphthalenes, focusing on spectroscopy, geometry, and vibrational energies. The photoelectron spectra (PES) of 1-CNN and 2-CNN were reported using the He I 21.2 eV resonance line in Utsunomiya et al. (1975) and Klasinc et al. (1983). The fluorescence excitation spectra of 1-CNN and 2-CNN were reported in Lahmani et al. (1993), showing very strong 0_0^0 transitions located at 31412 and 30874 cm^{-1}, respectively. The short lifetime of the 0^0 state for 1-CNN compared to the first vibronic levels was explained by the authors in terms of intersystem crossing favorable for this level. Later on, in 2013, Shivatare et al. (2013) reported the vibronic spectrum of the $S_1 \leftarrow S_0$ electronic transition of 1-CNN using two-color resonant two-photon mass-analyzed threshold ionization (MATI) spectroscopy showing the band origin at 31412 ± 2 cm^{-1}, causing a redshift due to the CN substitution to naphthalene along with several other bands originating due to the in-plane ring deformation vibrations. The cationic spectra of 1-CNN were recorded by ionizing via the 0^0, 33^1, 32^1, and 31^1 intermediate vibronic levels in the S_1 state of the neutral, providing the precise ionization energy of 1-CNN. Very recently, Bull et al. (2023) have reported on the photoionization dynamics of 1-CNN using synchrotron radiation, emphasizing that direct ionization is less probable compared to plasmon excitation followed by autoionization, where, upon absorption of the VUV photons, the molecule is photoexcited to the plasmon resonance, dominated by π–π^* transitions, which then undergoes prompt autoionization. Along with showing the photoelectron spectra, the authors have obtained the anisotropy parameter (β_2), further testified by scattering calculations. The predominantly negative β_2 values suggested that autoionization from the plasmon resonance is the dominant electron ejection channel for incoming photons, with energies between 11.5 and 16 eV. In addition to the spectroscopic studies of CNNs existing in the literature, recently Stockett et al. (2023) have reported the dissociation and radiative cooling rate coefficients of 1-CNN^+, showing that recurrent fluorescence (RF) stabilizes the vibrationally hot cation, in contradiction to the usual hypothesis of dissociation of small PAHs in the ISM. They showed that cations formed with up to 5 eV of internal vibrational energy can stabilize through RF without fragmenting. Finally, note that Kwon et al. (2003) reported the one-photon MATI spectrum of the cyanobenzene cation in the ground electronic state, obtaining high precision ionization energy and vibrational frequencies. In the present work, we provide the high-resolution threshold photoelectron spectra (TPES) of 1-CNN, 2-CNN, and cyanobenzene, as well as the state-selected cation dissociation pathways. Photoelectron spectra recorded as a function of photon energy allows us to extract the photoelectron kinetic energy distribution for any given interstellar radiation field (ISRF) up to the photon energies of 22.5 eV, with direct consequences for the ISM gas heating budget.

2. Experimental Method

The experiment has been carried out at the VUV undulator-based DESIRS beamline (Nahon et al. 2012) of the French synchrotron radiation facility SOLEIL. Horizontally polarized radiation was generated by an undulator whose higher harmonics were cut off by a few orders of magnitude by using a gas filter (Mercier et al. 2000) filled with Ar at 0.24 mbar to achieve high spectral purity in the photon energy range between 8 and 15.7 eV. Note that the 4s' absorption line of Ar in the gas filter was used for the absolute photon energy calibration. For higher photon energies beyond 15.7 eV, there is no need for the gas filter since the higher harmonics generated are very efficiently suppressed by the low dispersion/high flux 200 lines/mm grating that was used. The pure photon beam was then dispersed by an Eagle off-plane 6.65 m normal incidence monochromator, with an exit slit such that a photon flux of $\simeq 10^{13}$ photons/s was delivered to the sample, resulting in a photon energy resolution between 6 and 10 meV, corresponding to a photon energy varying from 8 to 24 eV. The monochromatized beam finally fed SAPHIRS, one of the permanent endstations at the DESIRS beamline.

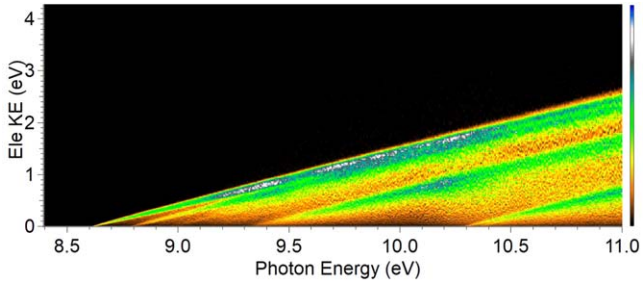

Figure 2. Two-dimensional photoelectron intensity matrix as a function of photon energy (horizontal axis) and electron kinetic energy (vertical axis) for 1-CNN. The matrix is mass selected on the parent ion. The photon energy was scanned from 8.4 to 11 eV with steps of 5 meV.

The commercially available samples of 1-CNN, 2-CNN, and cyanobenzene from Sigma Aldrich were placed directly in an in-vacuum stainless-steel oven without further purification and were heated to 90°C, 105°C, and 40°C, respectively. The vapor was seeded with He at a backing pressure of about 1 bar before expanding supersonically through a 100 μm nozzle inside the SAPHIRS molecular beam expansion chamber (Tang et al. 2015). The nozzle was kept 10°C hotter than the oven to avoid clogging the nozzle. The resulting free molecular jet was doubly skimmed and intersected the synchrotron radiation perpendicularly at the center of the ionization chamber. The ejected photoelectrons and photoions were extracted and accelerated in opposite directions by the DELICIOUS3 (Garcia et al. 2013) double imaging electron/ion coincidence (i^2PEPICO) spectrometer. The coincidence scheme is used here to mass filter the photoelectron images from which the mass-selected photoelectron spectra are obtained by Abel transform (Garcia et al. 2004). Scanning the photon energy allows a full mass-selected 2D matrix to be recorded (see Figure 2), encapsulating all the photoionization features. These include the TPES (Poully et al. 2010), which provide the cation spectroscopy with better and constant energy resolution than classical photoelectron spectroscopy at a fixed wavelength, at the expense of longer acquisition times. Because the photoelectron energy is fixed to a rather small value, the signal is only observed when the photon energy is resonant with a rovibronic state of the cation. Apart from collecting the threshold photoelectrons, another scan was performed over an extended photon energy from threshold to 22.5 eV. For this purpose, the extraction field was set to collect all photoelectrons with kinetic energies below ~12.5 eV, i.e., up to a photon energy of ~21 eV in the case of CNN (see Section 3.2). These photon energy scans were normalized to the photon flux, which was measured using an AXUV100, IRD photodiode, and by potential instabilities of the vaporization source by recording fast ion yield scans.

3. Results and Discussion

3.1. Photoelectron Spectra

Figure 2 shows a typical high-resolution 2D photoelectron matrix mass selected on the 1-CNN parent cation as a function of the photon energy and the kinetic energy of the photoelectrons. The photoelectron matrix contains a wealth of information that can be reduced in several ways, the first of which is to obtain the threshold photoelectron spectrum displayed in the three panels in Figure 3 for (a) 1-CNN, (b) 2-CNN, and (c) cyanobenzene, respectively. For either of the two isomers of

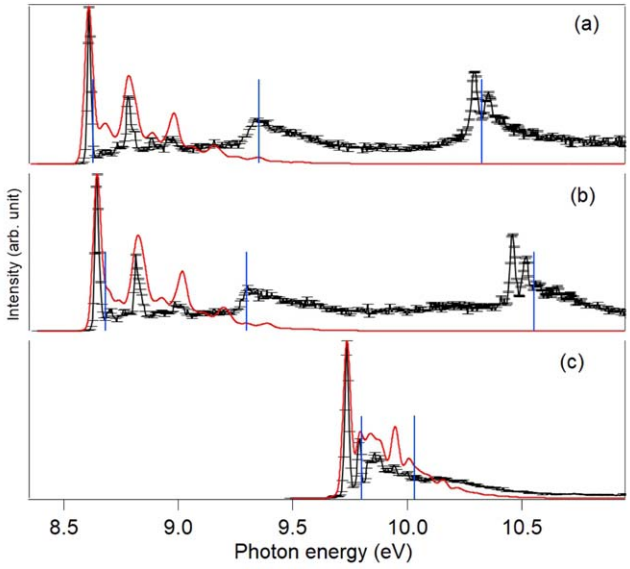

Figure 3. TPES of (a) 1-CNN, (b) 2-CNN, and (c) cyanobenzene. In each case, the black lines and markers are obtained experimentally with an overall resolution of 17 meV. The red curves correspond to the computed photoelectron spectrum for the ground electronic state of the cations. The experimental AIEs are obtained by fitting the 0_0^0 band; the vibrational progressions are discussed in the text. The blue vertical sticks correspond to the molecular orbitals obtained using the OVGF calculations.

CNN, transitions to the ground state and the first two excited states of the cations are visible. To understand the origin of these bands, the structures of the neutral molecule and the cation have been obtained at the DFT/M06-2X/aug-cc-pVTZ level of theory using the GAUSSIAN 16 Frisch et al. (2016) package, including vibrational frequencies. The calculated adiabatic ionization energies (AIEs) are obtained as the energy difference between the two minima and are corrected by the zero-point energy. The vibronic transitions to the cation ground state have been obtained through a Franck–Condon (FC) simulation at 0 K (see Figure A1 in the Appendix for 2-CNN) and convolved with the experimental resolution.

3.1.1. 1-CNN

The simulated $D_1[1A'']\ X^+ \leftarrow S_0$ *X* band shown in Figure 3(a) is shifted by −88 meV to match the experimental 0-0 origin band, which is not unexpected at this level of theory. It is dominated by the adiabatic transition, which is measured at 8.610 ± 0.005 eV, in good agreement with the AIE of 8.6127 ± 0.0006 eV reported by Shivatare et al. (2013) using the two-color resonant MATI technique, the recent synchrotron-based photoelectron spectroscopy work by Bull et al. (2023), which gave a value of 8.60 ± 0.03 eV, and with the two earlier works on He I PES quoting the ionization potential at 8.61 eV (Utsunomiya et al. 1975) and 8.59 eV (Klasinc et al. 1983; see Table A1 in the Appendix). From the simulations, it is inferred that the band around 8.77 eV corresponds to the in-plane ring deformation and the strong bands around 8.88 and 9.07 eV are due to the CC and CH stretching, respectively, whereas the band at 8.97 eV is a result of the C-CN stretching mode.

A lower resolution but wider energy range photoelectron spectrum is shown in Figure 4(a), along with the results of an outer valence Green's function (OVGF) calculation that yields the position of the vertical ionization transitions. An overall very good agreement is observed for the three highest

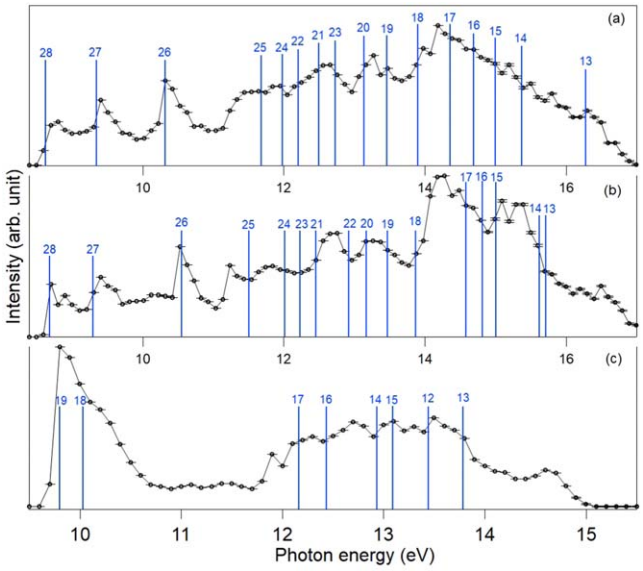

Figure 4. TPES up to about 17 eV in steps of 100 meV along with the blue vertical sticks showing the molecular orbitals obtained using the OVGF calculations for (a) 1-CNN, (b) 2-CNN, and (c) cyanobenzene. The statistical error bars are smaller than the symbol size.

molecular orbitals followed by a qualitative agreement for the others. The second and third bands at 9.37 and 10.3 eV match well with the photoelectron spectrum of Bull et al. (2023), which are assigned to $D_1[2A'']$ $A^+ \leftarrow S_0$ X transition and $D_2[3A'']$ $B^+ \leftarrow S_0$ X transition, respectively. The clear vibronic structure seen experimentally in the *B* band (second excited electronic state) allows us to report an accurate value for the third ionization energy, 10.294 ± 0.005 eV.

3.1.2. 2-CNN

The threshold photoelectron spectrum for 2-CNN is plotted in Figure 3(b) along with the FC simulation for the first electronic transition from which an experimental AIE is obtained at 8.645 ± 0.005 eV, in close agreement with the He I photoelectron spectrum reported by Utsunomiya et al. (1975) at 8.64 eV but differing from the 8.56 eV assigned by Klasinc et al. (1983; see Table A2 in the Appendix). The first AIE and the TPES are very similar to the 1-CNN isomer, within 40 meV, as are the positions of the *A* and *B* bands appearing at 9.3 and 10.46 eV, respectively. Clearly, neither the vibrational structure of the ground state nor the overall cation electronic structure are strongly isomer dependent. As in the case of 1-CNN, the *A* band is structureless while the *B* band shows vibrational structure, whose attribution falls out of the scope of this paper. Nevertheless, assuming the most intense band is the adiabatic transition, we give an AIE of 10.460 ± 0.005 eV for the *B* band. We also note that, in both isomers, there is a nonnegligible ion production within the FC gap, i.e., between electronic transitions, which is due to indirect processes like autoionization, known to contribute to TPES (Baer & Guyon 1986). Similar to that in 1-CNN, the vertical ionization transitions over an extended photon energy range spectrum are shown in Figure 4(b).

3.1.3. Cyanobenzene

The threshold photoelectron spectrum for cyanobenzene is shown in Figure 3(c) along with the result of the FC simulation for transitions to the cation ground state. The agreement is quite satisfactory and allows us to place the AIE at 9.736 ± 0.005 eV, in agreement with the 9.7288 ± 0.0006 eV reported by Kwon et al. (2003) obtained from one-photon MATI spectra and the 9.7315 ± 0.0002 eV by using two-color zero-kinetic-energy photoelectron spectroscopy reported by Araki et al. (1996; see Table A3 in the Appendix). When scanning over a wider energy range (see Figure 4(c)), the appearances of other excited states are seen, with one lying very close to the ground state, seen as a shoulder around 10.2 eV, in agreement with that reported by Klasinc et al. (1983) at 10.11 eV.

3.2. Contribution of Photoelectrons to the Gas Heating of the ISM

The heating of gases in galaxies due to the photoelectric effect was proposed by Spitzer (1948). When VUV photons interact with dust and nanograins, electrons with kinetic energy of a few eVs are emitted, which then give off their energies by collisions with the surrounding gas, resulting in heating of the gas. This is the major heating process in star-forming regions, protoplanetary disks, and ultraluminous infrared galaxies. Bakes & Tielens (1994) proposed theoretical models to estimate the contribution of nanograins and PAHs to the heating of interstellar gases depending on their sizes, typically up to 100 nm. Berné et al. (2022) used a recent model considering new data from laboratory measurements on PAHs, and comparison of the model results with observational diagnostics yielded good agreement over a wide range of radiation fields, concluding that PAH ionization is the main source of neutral gas heating in regions where they are present abundantly and subjected to VUV photons, such as near star-forming regions.

Figure 5 shows the extended 2D photoelectron matrix for 1-CNN along with two solid lines corresponding to two different ISRFs. Having a closer look at the 2D matrix, one can clearly see an increase in signal intensity on the third and fourth excited states over a broad energy range between 15.2 and 18 eV photon energy with the electron kinetic energy (KE) varying from 3.2 to 5 eV. According to the description of Bull et al. (2023), when 1-CNN is subjected to VUV radiation, particularly in the range of 11.5 and 16 eV, the molecule is photoexcited to the plasmon resonance, which then undergoes autoionization. Plasmon resonances occur due to a collective excitation of valence electrons to π^* states and are observed frequently in fullerene, graphene, and isolated PAHs. When above the ionization threshold, these excited states might decay by autoionization and are seen as resonances in the ion yields, with line widths reflecting their lifetime. For example, a previous study on the coronene cation by Bréchignac et al. (2014) clearly reveals that genuine autoionization features are visible as very sharp vertical lines in the 2D matrix at a definite photon energy rather than being spread over a few eVs, and that they decay into all the cation states at the same photon energy. In the present case, the total ion yields show a broad feature peaking at around 17 eV, which could be assigned to a plasmon resonance such as the one seen, for instance, in fullerene (Hertel et al. 1992). However, the photoelectron matrices such as those pictured in Figures 2 and 5 show that the maximum signal is found for all states (diagonal lines) at similar, if not equal, KEs—more reminiscent, strictly speaking,

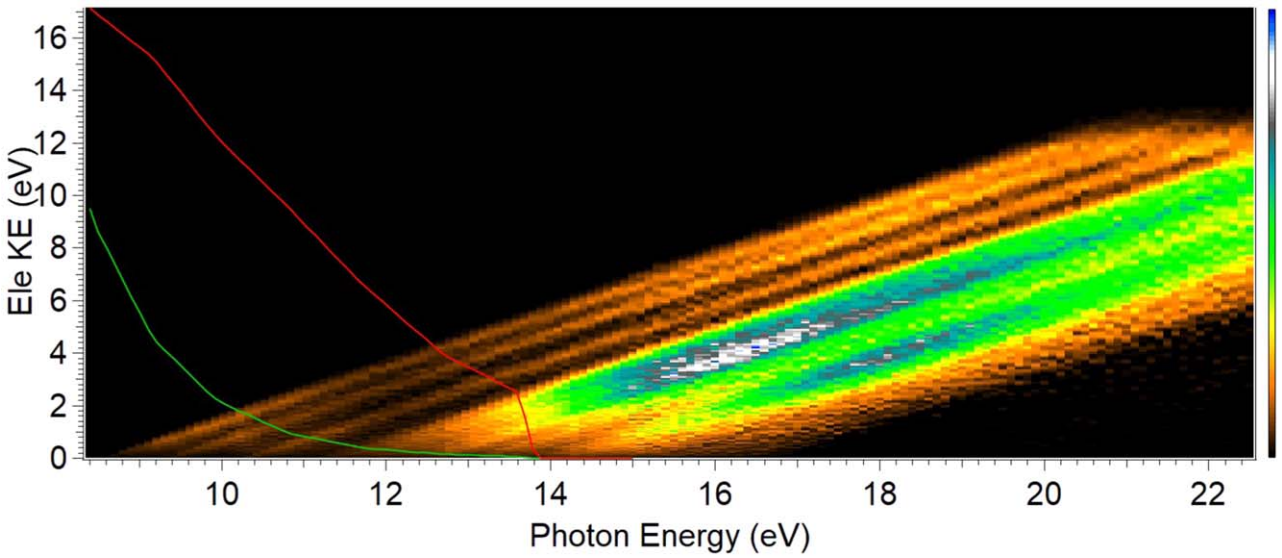

Figure 5. Two-dimensional photoelectron matrix of 1-CNN scanned over an extended photon energy. Two different ISRFs are shown; the green solid line is due to a 10,000 K blackbody radiation field, whereas the red solid line corresponds to a Galactic radiation field from Mathis et al. (1983).

of a shape resonance relaxation than of an autoionization process.

In the 2D matrix, performing an integration over the photon energy yields the KE distribution of the photoelectrons for a flat radiation field with a cutoff at $h\nu = 22.5$ eV, which corresponds to the shortest wavelength studied in this work (Figure 6(a) for 1-CNN and Figure 7(a) for 2-CNN). The KE distributions of the photoelectrons can further be used to model the contribution of these cyanoPAHs to the photoelectric heating for any radiation field in astrophysical environments. For the present study, we consider a 10,000 K blackbody radiation field (green solid line in Figure 5) and a Galactic radiation field estimated by Mathis et al. (1983; red solid line). By weighing the flat field distribution of Figure 6(a), we obtain the KE distribution of the photoelectrons emitted from 1- and 2-CNN when subjected to such ISRFs in the ISM. These e^- KE distributions are shown in Figures 6(b) and 7(b), where the green curve (multiplied six times for better visibility) in each case is due to the ISRF at 10,000 K and the red curve is due to the KE of the electrons for the incoming Galactic radiation field in Mathis et al. (1983). The intensity distribution of the ISRFs shows a sharp rise at very low photon energies, which then falls off exponentially. Convolution of the ISRFs at our experimental photon energy range shows the one at 10,000 K to decrease exponentially with an increase in photon energy, whereas the Galactic radiation field shows a sharp cutoff at 13.6 eV photon energy, corresponding to the ionization of atomic hydrogen. Indeed, PAHs are present in the H I region, and hence energetic photons above this value are absorbed. From the KE distributions, it is inferred that, for ionization of cyanonaphthalenes in the H I region by a typical ISRF, the maximum KE of the photoelectrons is about 5 eV, with the majority of photoelectrons having energies around 1.3 and 1.8 eVs. Such low mean electron energy values (∼few eVs) seem typical of PAHs regardless of their size and shape, as will be reported in a forthcoming article by some of the authors (Hrodmarsson et al. (to be submitted)). To get an idea about the mean KE of the photoelectrons emitted from 1-CNN when exposed to different ISRFs, we have plotted the mean KE as a function of the mean photon energy of the ISRFs, which is displayed in Figure 8.

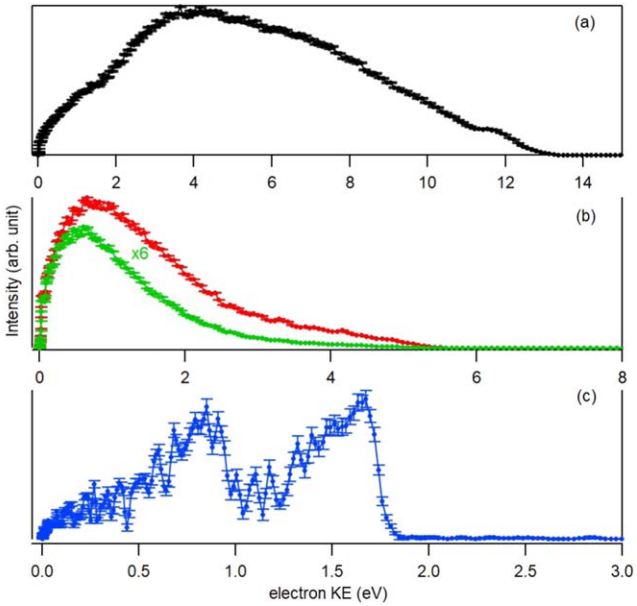

Figure 6. e^- KE distribution for 1-CNN: (a) corresponding to a flat radiation field with a cutoff at 22.5 eV; (b) where the green curve (multiplied by six for better visibility) is due to the 10,000 K blackbody radiation field and the red curve is for a Galactic radiation field (Mathis et al. 1983); and (c) at the Lyman α emission line. Note that the electron KE range is different for each panel.

The four points correspond to blackbody radiation fields at different temperatures and all with a cutoff at 13.6 eV. Initially, with the increase in temperature of the radiation field, the mean electron KE increases but then the curve tends to saturate for higher temperatures, indicating that the majority of electrons emitted are within the first two eVs. A similar kind of KE distribution is obtained for the photoelectrons emitted from cyanobenzene (shown in Figure A2 of the Appendix) except that the maximum KE of the photoelectrons emitted is about 3.8 eV, with the intensity being maximum around 0.5 eV. It is noteworthy to mention that the present 2D matrix can be exploited to obtain the KE of the photoelectrons emitted from PAHs due to any incoming ISRF and, in turn, can be used to estimate the heating effect in the ISM. So far, the majority of

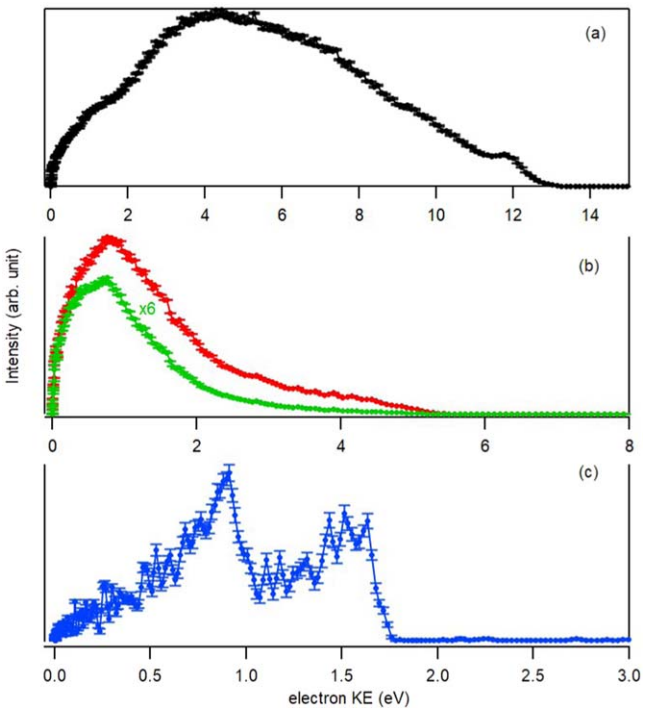

Figure 7. KE distribution of electrons emitted from 2-CNN: (a) for a flat radiation field up to 22.5 eV; (b) for the two ISRFs (green and red curves correspond to 10,000 K blackbody and a Galactic radiation field, respectively) shown in Figure 5 (the green curve is multiplied by six for better visibility); and (c) at 10.2 eV, Lyman α emission line.

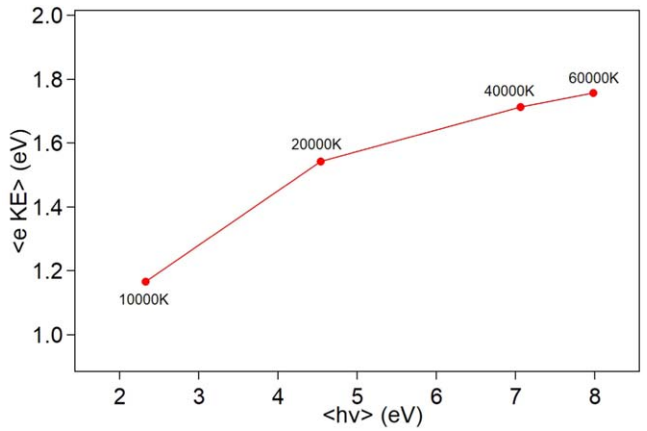

Figure 8. Mean KE of electrons emitted from 1-CNN when exposed to different ISRFs.

studies on the heating of gases have been based on theoretical predictions, and such experimental measurements can serve as important input for models like that of Berné et al. (2022), providing accurate information for the contribution of PAHs in maintaining the temperature balance in the ISM.

The UV field close to a star is dominated by atomic emission lines, mainly the H I Lyα emission line at 121.6 nm (10.2 eV). This line deserves special attention because of its significantly high intensity in the galactic environment, as high as 90% of the total far-UV flux being contributed by the Lyα emission in some cases (Heays et al. 2017). It is thus important to observe the spectral features of these PAH derivatives under the influence of the Lyα emission line. Going back to the 2D PES matrix in Figure 2, instead of integrating over the entire photon energy, if we perform a vertical slicing at 10.2 eV, we extract the photoelectron spectra plotted in Figures 6(c) and 7(c) for 1-CNN and 2-CNN, respectively. The two structured and strong bands correspond to the ground and first electronically excited state of the cations, and this is the first ever precise measurement of the photoelectrons from cyanoPAHs around the H I Lyα emission line. The maximum KE of these photoelectrons would be KE $= h\nu -$ AIE, i.e., 1.56 eV. In the case of cyanobenzene, only one structured band is observed (Figure A2(c) in the Appendix), corresponding to the ground electronic state cation with a maximum KE of 0.46 eV.

3.3. Photoionization Cross Sections and Photorates

In the absence of absolute measurements of photoionization cross sections, total ion yields are often scaled to derive them in order to compute photorates for use in astrochemical models (Heays et al. 2017; Hrodmarsson & van Dishoeck 2023). In this work, the total ion yields can be obtained by summing over all the photoion signals in the 2D photoelectron intensity matrices for 1-CNN and 2-CNN. While no absolute photoionization cross sections of 1-CNN and 2-CNN have been recorded previously, absolute cross sections have been measured for related molecules, such as benzene (see Zhou et al. 2009 and references therein) and cyanobenzene (Huang et al. 2021), naphthalene, and 1-methylnaphthalene (Jin et al. 2020). Comparisons of the cross sections of benzene and cyanobenzene reveal that replacing a H atom in benzene with a cyano group appears to increase the absolute cross section from 45 to 60 Mb at 12 eV (33% increase). We can thus provide a tentative scaling of the recorded total ion yields of 1-CNN and 2-CNN to be around one-third larger than that of naphthalene from Jin et al. (2020) before the onset of plasmon resonance. The scaled cross sections of 1-CNN and 2-CNN are plotted together with the cross sections of naphthalene and 1-metylnaphthalene in Figure A6 of the Appendix. These scaled cross sections, which we can estimate accurately within 30%, are then used to compute the photorates under various radiation fields and from cosmic ray ionization-induced VUV irradiation. The details of the calculations have been given previously (Heays et al. 2017; Hrodmarsson & van Dishoeck 2023). These rates are presented in Table A4 of the Appendix.

3.4. Dissociation of CyanoPAHs

PAHs may undergo unimolecular reactions in astrophysical environments upon excitation or ionization after absorbing the UV photons emitted by hot stars. In the case of small PAHs, H loss and C_2H_2 loss are the two most dominant channels of fragmentation for either neutral and monocharged or multicharged cationic PAHs (Jochims et al. 1994; West et al. 2018). In the present study, we have performed measurements to investigate the different dissociation channels obtained from the cyanonaphthalene cation (m/z 153). The five different observed primary dissociation channels from the 2-CNN cation are shown in black font in Figure 9. The cation can lose a H atom, forming $C_{10}H_6CN^+$. In the time-of-flight mass spectrum (see Figures A3 and A4 in the Appendix), the peak at m/z 127 could be due to the formation of $C_8H_5CN^+$ accompanied by the loss of acetylene (C_2H_2) or the result of breaking the C-CN bond, leading to the production of $C_{10}H_7^+$ ion (CN loss). The peak at m/z 126 is due to HCN loss from the cation. There can also be loss of the H_2

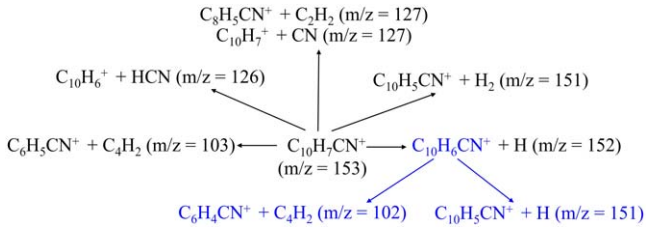

Figure 9. Observed dissociation pathways of 2-CNN.

molecule, giving rise to $C_{10}H_5CN^+$. The parent ion might also dissociate to form neutral butadiyne (C_4H_2) along with the detection of $C_6H_5CN^+$ on the ion detector. Apart from these primary fragmentation channels, the parent ion, after losing a H atom, i.e., the fragment ion $C_{10}H_6CN^+$, can further undergo dissociation into two different pathways, which are written in blue font in Figure 9. Recently, Kamer et al. 2023 reported on the fragmentation of cyanobenzene, highlighting the seven major dissociation channels and a few other channels of lower fractional abundances, which includes the H loss channel.

Figure 10 displays the breakdown diagram of 2-CNN^+, i.e., the molar fraction of parent and fragments as a function of the energy deposited into the neutral molecule. The symbols show the experimentally obtained fractional abundances of the parent and fragment ions, whereas the solid lines are obtained using the MassKinetics program (Drahos & Vékey 2001), based on the Rice–Ramsperger–Kassel–Marcus (RRKM) statistical model, to fit the experimental curves. The model considers thermal effects in the neutral parent as well as kinetic effects in the dissociation of the cation to yield appearance energies at 0 K, i.e., free of experimental bias. By far the main dissociation channel in our energy range corresponds to the loss of $HCN/C_2H_2/CN$. However, we note that m/z 126 and 127 cannot be fully separated in our spectrometer due to the ion KE release that broadens the time-of-flight peaks. Therefore, we cannot quantify the individual contribution of $HCN/C_2H_2/CN$ loss to Figure 10. Similarly, the peaks at m/z 102 and 103 also overlap with very low yield, which are again taken together to generate the figure. The extraction of the fragment appearance energies from Figure 10 is not trivial since temperature and kinetic effects need to be taken into account. For the former, we assume that all vibrational modes of the neutral molecule are thermalized while, for the latter, we use the RRKM theory, where the transitional modes are treated with the rigid activation complex model, which consists of multiplying the transitional frequencies by a given factor as a means to adjust the entropy of the transition state (Baer & Hase 1996). The vibrational frequencies of the parent molecule used as an input to the model were calculated at the M06-2X/aug-cc-pVTZ level of theory, while raytracing simulations were performed to obtain the experimental decomposition time, i.e., the time during which the parent ions are accelerated in the ionization region of DELICIOUS3 (1.6 μs). The vibrational temperature of 100 K is manually adjusted to best fit the experimental curves, and this value is consistent with the cooling from the adiabatic expansion. Using the experimentally obtained AIE of 2-CNN (Section 3.1.2), the photon energies have been converted to the ion internal energies for the RRKM modeling. From Figure 10, it is seen that the model works very well for the parent ion decay while, for the fragments, the model works best for the lower photon energies, perhaps due to the larger signal-to-noise ratio and the larger uncertainties at higher

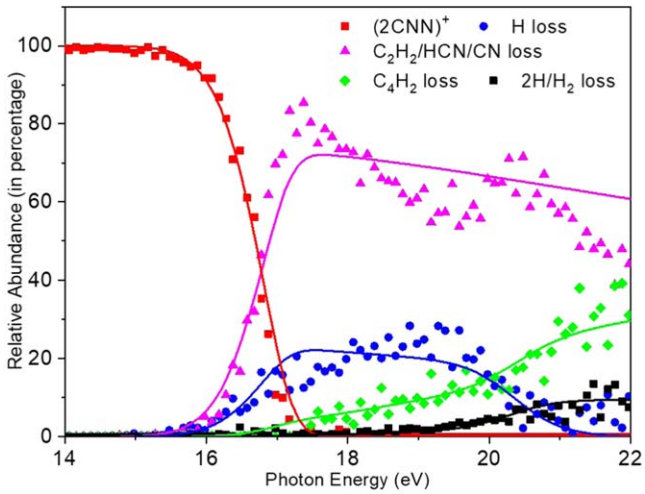

Figure 10. Breakdown diagram for 2-CNN. The solid lines are obtained using RRKM modeling.

excess energies linked to the number of pathways opened or deviations from statistical behavior.

For C_4H_2 loss, there is a change in slope at 20 eV, which could be attributed to butadiyne loss after the loss of the H atom from $2CNN^+$. A similar change in slope is seen for $H_2/2H$ loss, which follows the same mechanism as above. Such a slope change in the model has been reported by West et al. (2012) for the case of naphthalene. The first fragmentation channel to open involves H loss. The activation energies (E_0) obtained from the model are tabulated in Table 1. A comparison has been made with the E_0 values for CNN^+ reported by West et al. (2019) using a collision-induced dissociation mechanism, where the authors mentioned the two most prominent channels of dissociation, HCN loss and C_2H_2 loss, and with the unsubstituted naphthalene reported by West et al. (2012). As the peaks at m/z 126 and 127 could not be separated, we have quoted the same E_0 values for HCN and C_2H_2 loss. In the case of C_2H_2 loss, we have a close agreement with West et al. (2019), whereas for HCN loss, we have a higher E_0 value, which could be a result of not being able to separate the two peaks and eventually being unable to fit the HCN loss curve separately. The two humps seen in the experimental breakdown curve (pink solid triangles) could be due to the two most prominent but unresolved dissociation channels, HCN and C_2H_2. Stockett et al. (2023), by using a cryogenic ion storage ring at 13K, have reported an E_0 value of 3.16 eV for the HCN loss from 1-CNN^+, the most abundant dissociation channel observed. The discrepancy with our derived value is likely due to differences in the experimental decomposition time, with ours being orders of magnitude shorter, amplifying the errors due to the difficulty in accurately describing the transition state. Within experimental limitations, it is seen that CN substitution to naphthalene causes a slight decrease in the appearance threshold of some of the fragments. Note that one such limitation is the large kinetic shift predicted in our experimental setup, i.e., the extra energy required to detect a fragmentation channel within the short residence time ($\sim\mu$s) in the acceleration region of the spectrometer, which was obtained from the RRKM model to be about 3.0 eV. Indeed, large kinetic shifts render the extrapolation to thermochemical values more imprecise. A very similar breakdown diagram, and therefore activation energies, has been obtained for 1-CNN^+, which is shown in Figure A5 of the Appendix. The activation

Table 1
Activation Energies (E_0/eV) for the Dissociation Channels from 1-CNN$^+$ and 2-CNN$^+$, Comparison with Data from the Literature (Stockett et al. (2023) for 1-CNN$^+$ and West et al. (2019) for 2-CNN$^+$) along with the Values for Unsubstituted Naphthalene (West et al. 2012)

	This work		Literature		
			Stockett et al. (2023)	West et al. (2019)	West et al. (2012)
Reaction	1-CNN$^+$	2-CNN$^+$	1-CNN$^+$	2-CNN$^+$	$C_{10}H_8^+$
$C_{10}H_7CN^+ \rightarrow C_{10}H_6CN^+ + H$	3.76	3.76	⋯	⋯	4.2 ± 0.04
$C_{10}H_7CN^+ \rightarrow C_8H_5CN^+ + C_2H_2$			⋯	≈4	4.12 ± 0.05
$C_{10}H_7CN^+ \rightarrow C_{10}H_7^+ + CN$	3.87	3.83	⋯	⋯	⋯
$C_{10}H_7CN^+ \rightarrow C_{10}H_6^+ + HCN$			3.16	2.5-3	⋯
$C_{10}H_7CN^+ \rightarrow C_6H_5CN^+ + C_4H_2$	4.45	4.43	⋯	⋯	4.27 ± 0.07
$C_{10}H_7CN^+ \rightarrow C_{10}H_5CN^+ + H_2$	4.62	4.65	⋯	⋯	4.72 ± 0.06
$C_{10}H_6CN^+ \rightarrow C_6H_4CN^+ + C_4H_2$	3.7	3.7	⋯	⋯	3.69 ± 0.26
$C_{10}H_6CN^+ \rightarrow C_{10}H_5CN^+ + H$	3.45	3.45	⋯	⋯-	3.2 ± 0.13

Table 2
Percentage Yield of Parent and Fragment Ions for 2-CNN under the Influence of Different Radiation Fields Cutting Off at 13.6 eV

Ions	10,000 K	20,000 K	40,000 K	60,000 K
$(2\text{-CNN})^+$	99.8	99.8	99.7	99.7
H loss	0.06	0.1	0.2	0.2
C_2H_2/HCN/CN loss	0.01	0.01	0.02	0.02
C_4H_2 loss	0.01	0.01	0.01	0.01
$2H/H_2$ loss	0.07	0.08	0.08	0.08

energies for the dissociation pathways of CNN cations were mostly lower than naphthalene except for butadiyne loss, where an additional 0.18 and 0.16 eV had to be invested to open the channel as well as for the second H loss where 0.25 eV more was required.

The present experimental measurements for 2-CNN have been further exploited to obtain the percentage yield of the parent and fragment ions when subjected to different radiation fields in the ISM (see Table 2). By setting the dissociation time to the accepted maximum of 10 ms (beyond which radiative decay kicks in) and using the transition state entropy and appearance energies extracted from the RRKM modeling of our breakdown diagram, the total not-state-selected fragmentation rates in an astrophysical environment can be estimated from the mass-selected ion yields at a given ISRF. It is seen that the parent ion survival rate is 99.7%–99.8% under the influence of the photon fields with a cutoff at 13.6 eV, whereas the contribution of the $C_{10}H_6CN^+$ ion after the parent has lost one H atom is 0.1%–0.2% and the probability of forming the other fragments is less than 0.1%.

4. Conclusions

Exploiting the photoelectron–photoion coincidence technique, we have obtained the mass-selected photoelectron signal as a function of kinetic and photon energy. From these data, high-resolution TPES for cyano-substituted naphthalene and cyanobenzene cations in the VUV range have been extracted and compared to simulated spectra and existing literature, leading in all cases to excellent agreement. New accurate adiabatic ionization values are reported for the second excited states of both CNN and for the first ionization energy of 2-CNN. The adiabatic ionization energies increased by about 0.5 eV due to the addition of the cyano group compared to unsubstituted naphthalene and unsubstituted benzene.

The 2D data on the photoelectron matrices have been further exploited to provide the photoelectron KE distributions for any given incoming ISRF in order to estimate the contribution of these molecules to photoelectric heating. It is observed that the average KEs are rather low, between 1 and 2 eV. The matrices show that, within our photon energy range, a major reason for the ejection of slow photoelectrons is the broad and intense resonance peaking at $h\nu = \sim 17$ eV. Close inspection shows the photoelectron partial cross sections peaking at similar KEs, pointing to a continuum shape resonance trapping the outgoing photoelectron in the PAH potential for a subfemtosecond time, rather than a collective excitation to π^* orbitals that then would decay by autoionization. In any case, production of slow photoelectrons will enrich the ensuing chemistry by processes such as dissociative attachment, where the slow photoelectrons can attach to other neutral molecules, forming transient molecular anions that then undergo fragmentation.

We report estimated absolute photoionization rates for several relevant ISRFs by comparison to known absolute ionization cross sections of similar systems.

Finally, exploring the dissociation channels of the cyano-substituted naphthalenes reveals that the addition of the CN group does not significantly change the overall fragmentation pattern, nor the energetics. Indeed, the slightly lower critical energies of the substituted naphthalenes are compensated by their slightly larger adiabatic ionization energies with respect to naphthalene. Further, the position of the cyanide group on the aromatic ring does not cause any appreciable change to the activation energies for opening up the fragmentation channels. Under the influence of the different radiation fields in the H I region of the astrophysical environment, it is seen that the parent ion remains predominantly very stable for a long decomposition time up to 10 ms, a time frame beyond which the cation would relax by emission of infrared radiation rather than by fragmentation.

Acknowledgments

We warmly thank the SOLEIL general staff for providing beamtime under projects 99210274 and 99220154. We are especially grateful to Jean-Francois Gil for his technical help

around the SAPHIRS setup. We extend our sincere thanks to Denis Lesage for his help with the RRKM modeling.

Appendix

Figure A1 shows the simulated Franck–Condon intensities for 2-CNN. Figure A2 shows the eletron KE distributions for cyanobenzene whereas Figures A3 and A4 are the 2D histograms of the coincidence signal and time-of-flight mass spectra of 1-CNN, respectively. Figure A5 depicts the breakdown diagram for 1-CNN and Figure A6 the scaled total ion yields for 1- and 2-CNN. The adiabatic ionization energies for 1-CNN, 2-CNN and cyanobenzene are tabulated in Tables A1, A2, and A3, respectively, whereas Table A4 provides the photorates for the two cyanonaphthalenes under different radiation fields.

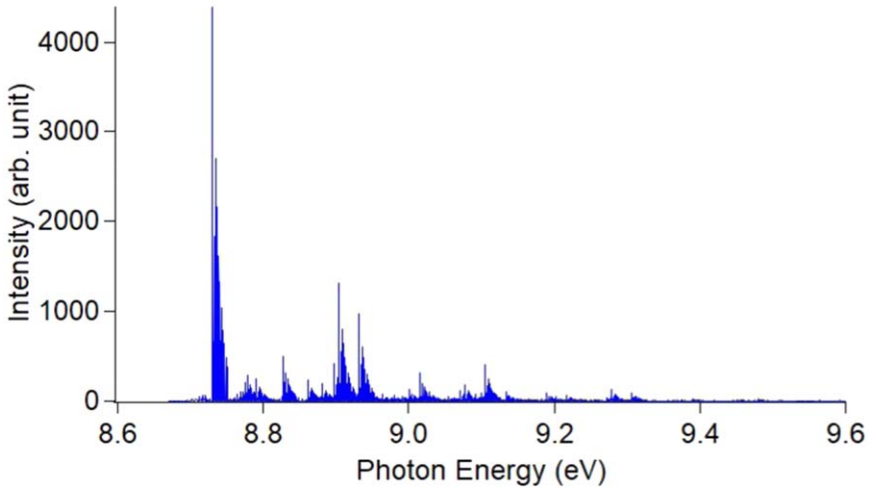

Figure A1. Simulated Franck–Condon intensities for 2-CNN where each stick corresponds to an individual vibronic transition.

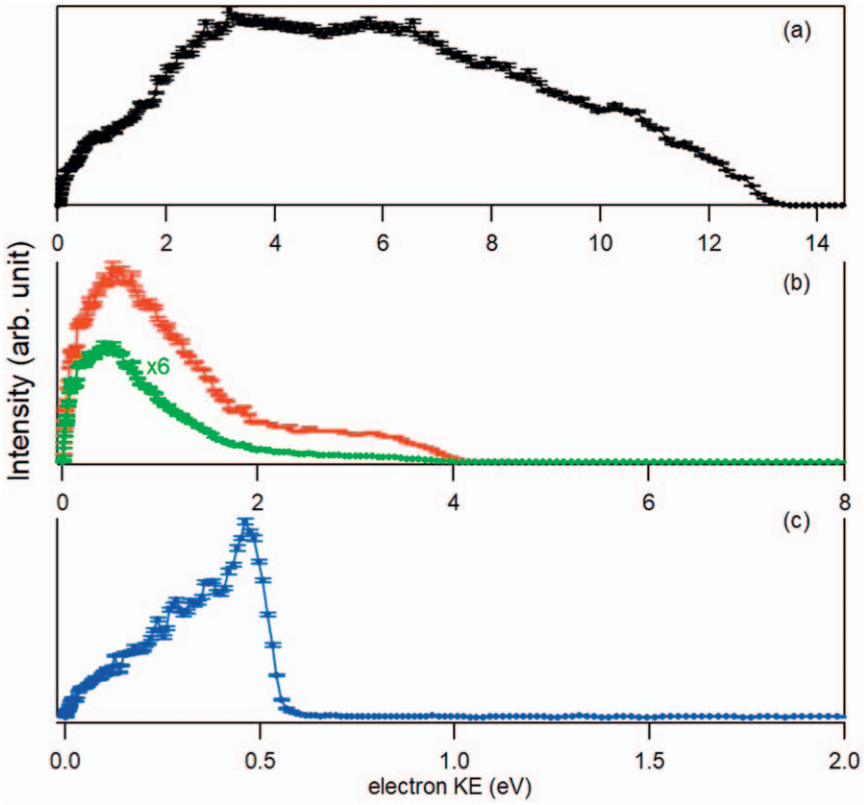

Figure A2. e^- KE distribution for cyanobenzene: (a) for a flat radiation field with a cutoff at 22.5 eV; (b) for two different ISRFs (the green curve is due to the 10,000 K blackbody radiation field, whereas the red curve corresponds to a galactic radiation field; the green curve is multiplied by six for better visibility); and (c) at the Lyman α emission line.

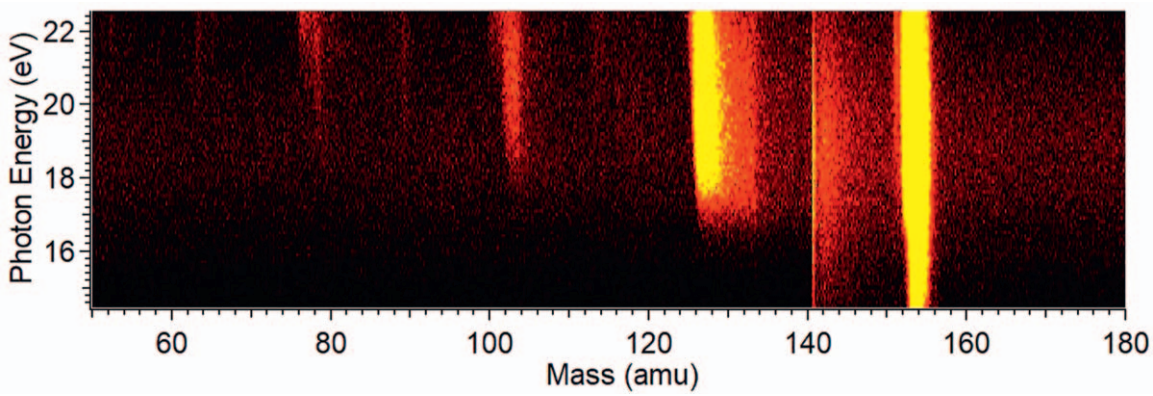

Figure A3. Two-dimensional histogram of the coincident signal as a function of m/z on the horizontal axis and photon energy on the vertical axis, between 14.5 and 22.5 eV.

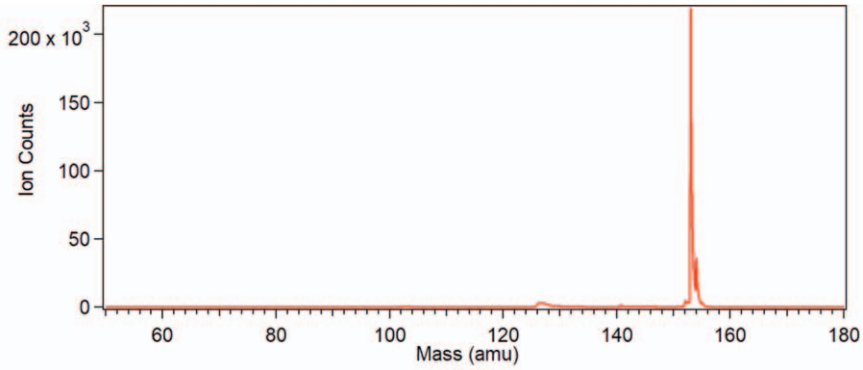

Figure A4. Time-of-flight mass spectra of 1-CNN recorded over 17.5 to 22.5 eV photon energies.

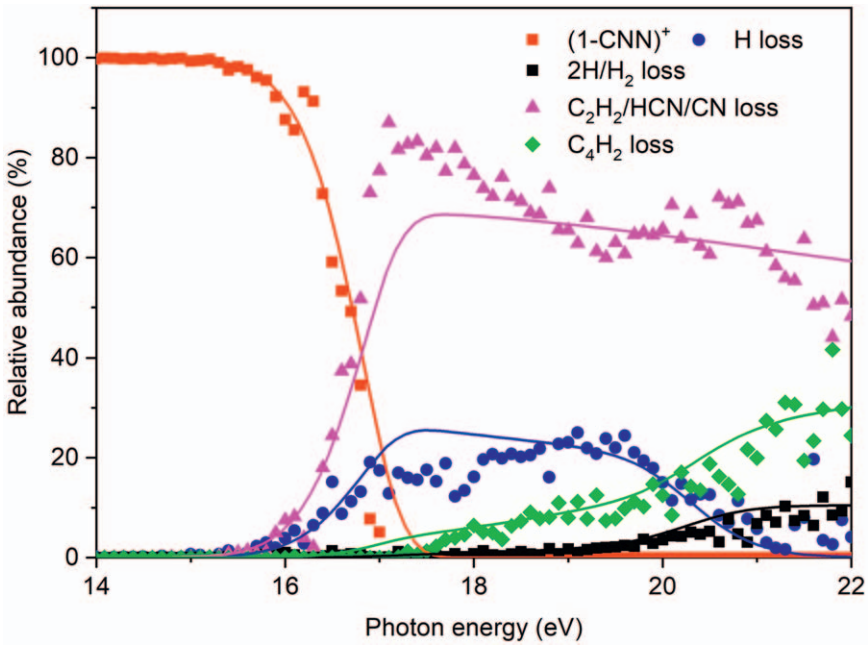

Figure A5. Breakdown diagram for 1-CNN along with the solid lines obtained from RRKM modeling.

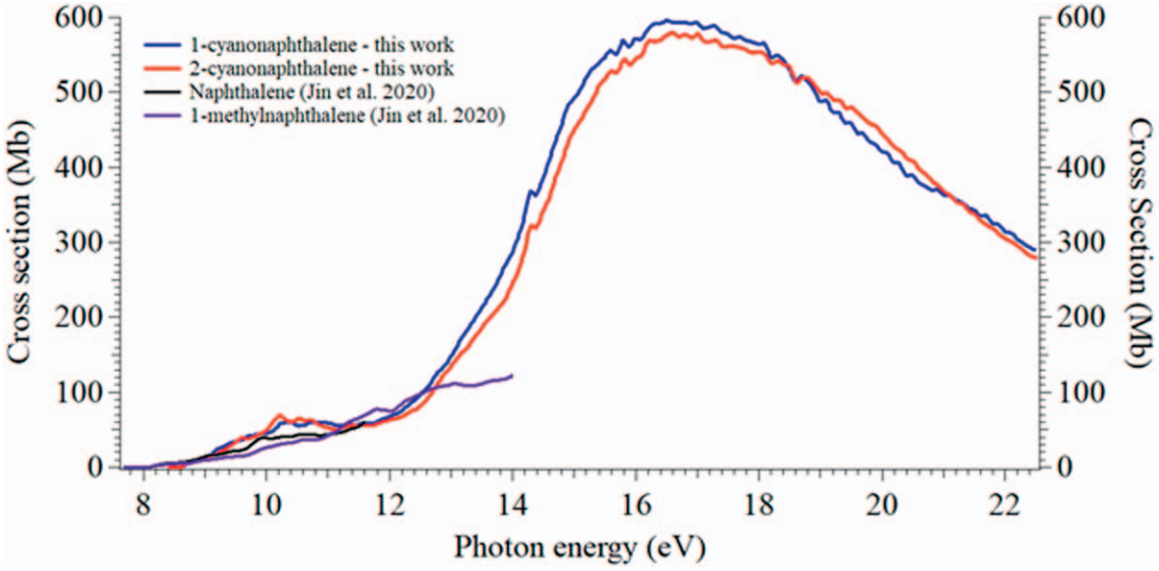

Figure A6. Scaled total ion yields of 1-CNN and 2-CNN along with the recorded absolute photoionization cross sections of Jin et al. (2020).

Table A1
Adiabatic Ionization Energies of 1-CNN from This Work and Comparison with Those Reported in the Literature

1-CNN	AIE (eV)
This work	8.610 ± 0.005
Bull et al. (2023)	8.60 ± 0.03
Shivatare et al. (2013)	8.6127 ± 0.0006
Klasinc et al. (1983)	8.59
Utsunomiya et al. (1975)	8.61

Table A2
Similar to Table A1, Except for 2-CNN

2-CNN	AIE (eV)
This work	8.645 ± 0.005
Klasinc et al. (1983)	8.56
Utsunomiya et al. (1975)	8.64

Table A3
Similar to Table A1, Except for Cyanobenzene

Cyanobenzene	AIE (eV)
This work	9.736 ± 0.005
Kwon et al. (2003)	9.7288 ± 0.0006
Araki et al. (1996)	9.7315 ± 0.0002

Table A4
Computed Photorates (sec^{-1}) under Different Radiation Fields Using the Scaled Cross Section in Figure A6

Different Radiation Fields	1-CNN	2-CNN
ISRF	4.13E-09	4.01E-09
Mathis1983	3.02E-09	2.91E-09
Habing 1968	2.10E-09	1.99E-09
4000 K	5.68E-12	5.69E-12
10,000 K	7.39E-10	7.32E-10
20,000 K	3.52E-09	3.39E-09
Lyα	8.78E-09	1.07E-08
Solar	5.0E-10	5.54E-10
TW-Hya	6.38E-09	7.41E-09
Cosmic ray ionization	4.46E-13	4.65E-13

ORCID iDs

Madhusree Roy Chowdhury https://orcid.org/0009-0004-5607-6781
Gustavo A. Garcia https://orcid.org/0000-0003-2915-2553
Helgi R. Hrodmarsson https://orcid.org/0000-0002-9613-5684
Jean-Christophe Loison https://orcid.org/0000-0001-8063-8685
Laurent Nahon https://orcid.org/0000-0001-9898-5693

References

Agúndez, M., Marcelino, N., Tercero, B., & Cernicharo, J. 2023, A&A, 677, L13
Allamandola, L. J., Tielens, A. G. G. M., & Barker, J. R. 1985, ApJL, 290, L25
Araki, M., Sato, S. i., & Kimura, K. 1996, JPhCh, 100, 10542
Baer, T., & Guyon, P. M. 1986, JChPh, 85, 4765
Baer, T., & Hase, W. L. 1996, Unimolecular Reaction Dynamics (Oxford: Oxford Univ. Press),
Bakes, E. L. O., & Tielens, A. G. G. M. 1994, ApJ, 427, 822
Bakes, E. L. O., Tielens, A. G. G. M., Charles, W. B., Jr., Hudgins, D. M., & Allamandola, L. J. 2001, ApJ, 560, 261
Belloche, A., Garrod, R. T., Müller, H. S. P., & Menten, K. M. 2014, Sci, 345, 1584
Berné, O., Foschino, S., Jalabert, F., & Joblin, C. 2022, A&A, 667, A159
Boersma, C., Bregman, J., & Allamandola, L. J. 2016, ApJ, 832, 51
Boersma, C., Bregman, J., & Allamandola, L. J. 2018, ApJ, 858, 67
Bottinelli, S., Ceccarelli, C., Lefloch, B., et al. 2004, ApJ, 615, 354
Brandl, B. R., Bernard-Salas, J., Spoon, H. W. W., et al. 2006, ApJ, 653, 1129
Bréchignac, P., Garcia, G. A., Falvo, C., et al. 2014, JChPh, 141, 164325
Bull, J. N., Bolognesi, P., Anstöter, C. S., et al. 2023, JChPh, 158, 241101
Burkhardt, A. M., Lee, K. L. K., Changala, P. B., et al. 2021a, ApJL, 913, L18
Burkhardt, A. M., Loomis, R. A., Shingledecker, C. N., et al. 2021b, NatAs, 5, 181
Canelo, C. M., Friaça, A. C. S., Sales, D. A., Pastoriza, M. G., & Ruschel-Dutra, D. 2018, MNRAS, 475, 3746
Cernicharo, J., Agúndez, M., Cabezas, C., et al. 2021, A&A, 649, L15
Cox, N. L. J., Pilleri, P., Berné, O., Cernicharo, J., & Joblin, C. 2015, MNRAS: Letters, 456, L89
Cravens, T. E., & Dalgarno, A. 1978, ApJ, 219, 750
Croiset, B. A., Candian, A., Berné, O., & Tielens, A. G. G. M. 2016, A&A, 590, A26
Dalgarno, A. 2006, PNAS, 103, 12269
Drahos, L., & Vékey, K. 2001, JMSp, 36, 237
Frisch, M. J., Trucks, G. W., Schlegel, H. B., et al. 2016, Gaussian 16 Revision C.01, Gaussian Inc. Wallingford CT

Garcia, G. A., Cunha de Miranda, B. K., Tia, M., Daly, S., & Nahon, L. 2013, RScI, 84, 053112
Garcia, G. A., Nahon, L., & Powis, I. 2004, RScI, 75, 4989
García-Bernete, I., Rigopoulou, D., Alonso-Herrero, A., et al. 2022, A&A, 666, L5
Heays, A. N., Bosman, A. D., & van Dishoeck, E. F. 2017, A&A, 602, A105
Hertel, I. V., Steger, H., de Vries, J., et al. 1992, PhRvL, 68, 784
Hrodmarsson, H. R., & van Dishoeck, E. F. 2023, A&A, 675, A25
Huang, J., Huang, C., Wu, X., et al. 2021, JChPh, 154, 244301
Jin, H., Yang, J., & Farooq, A. 2020, RCMS, 34, e8899
Joblin, C., Leger, A., & Martin, P. 1992, ApJL, 393, L79
Jochims, H. W., Ruhl, E., Baumgartel, H., Tobita, S., & Leach, S. 1994, ApJ, 420, 307
Kamer, J., Schleier, D., Donker, M., et al. 2023, PCCP, 25, 29070
Klasinc, L., Kovac, B., & Gusten, H. 1983, Pure Appl. Chem., 55, 289
Knight, C., Peeters, E., Wolfire, M., & Stock, D. J. 2021, MNRAS, 510, 4888
Kwon, C. H., Kim, H. L., & Kim, M. S. 2003, JPCA, 107, 10969
Lahmani, F., Bréhéret, E., Zehnacker-Rentien, A., & Ebata, T. 1993, J. Chem. Soc., Faraday Trans., 89, 623
Leach, S. 1986, JESRP, 41, 427
Lee, K. L. K., McGuire, B. A., & McCarthy, M. C. 2019, PCCP, 21, 2946
Leger, A., & Puget, J. L. 1984, A&A, 137, L5
Li, A., & Draine, B. T. 2002, ApJ, 576, 762
Maaskant, K. M., Min, M., Waters, L. B. F. M., & Tielens, A. G. G. M. 2014, A&A, 563, A78
Mathis, J. S., Mezger, P. G., & Panagia, N. 1983, A&A, 128, 212
McGuire, B. A., Burkhardt, A. M., Kalenskii, S., et al. 2018, Sci, 359, 202
McGuire, B. A., Loomis, R. A., Burkhardt, A. M., et al. 2021, Sci, 371, 1265
Menéndez-Delmestre, K., Blain, A. W., Smail, I., et al. 2009, ApJ, 699, 667
Mercier, B., Compin, M., Prevost, C., et al. 2000, JVSTA, 18, 2533
Montillaud, J., Joblin, C., & Toublanc, D. 2013, A&A, 552, A15
Nahon, L., de Oliveira, N., Garcia, G. A., et al. 2012, JSynR, 19, 508
Oey, M. S., López-Hernández, J., Kellar, J. A., et al. 2017, ApJ, 844, 63
Ohsawa, R., Onaka, T., Sakon, I., et al. 2012, ApJL, 760, L34
Poully, J. C., Schermann, J. P., Nieuwjaer, N., et al. 2010, PCCP, 12, 3566
Prasad, S. S., & Tarafdar, S. P. 1983, ApJ, 267, 603
Rapacioli, M., Joblin, C., & Boissel, P. 2005, A&A, 429, 193
Sellgren, K., Uchida, K. I., & Werner, M. W. 2007, ApJ, 659, 1338
Shivatare, V., Tzeng, S. Y., & Tzeng, W. B. 2013, CPL, 558, 20
Sita, M. L., Changala, P. B., Xue, C., et al. 2022, ApJL, 938, L12
Spitzer, L. J 1948, ApJ, 107, 6
Steglich, M., Bouwman, J., Huisken, F., & Henning, T. 2011, ApJ, 742, 2
Stock, D. J., & Peeters, E. 2017, ApJ, 837, 129
Stockett, M. H., Bull, J. N., Cederquist, H., et al. 2023, NatCo, 14, 395
Taha, A. S., Labadie, L., Pantin, E., et al. 2018, A&A, 612, A15
Tang, X., Garcia, G. A., Gil, J. F., & Nahon, L. 2015, RScI, 86, 123108
Tielens, A. 2008, ARA&A, 46, 289
Tielens, A. G. G. M. 2011, EAS Publ. Ser., 46, 3
Topchieva, A., Wiebe, D., & Kirsanova, M. S. 2018, RAA, 18, 091
Utsunomiya, C., Kobayashi, T., & Nagakura, S. 1975, Bull. Chem. Soc. Jpn., 48, 1852
Verstraete, L. 2011, The Role of PAHs in the Physics of the Interstellar Medium (Les Ulis: EDP Sciences), 415
Wakelam, V., & Herbst, E. 2008, ApJ, 680, 371
West, B., Joblin, C., Blanchet, V., et al. 2012, JPCA, 116, 10999
West, B., Rodriguez Castillo, S., Sit, A., et al. 2018, PCCP, 20, 7195
West, B. J., Lesniak, L., & Mayer, P. M. 2019, JPCA, 123, 3569
Zhang, H., Telesco, C. M., Pantin, E., et al. 2017, MNRAS, 465, 2983
Zhou, Z., Xie, M., Wang, Z., & Qi, F. 2009, RCMS, 23, 3994